

Current Biology

Dissociation between Postrhinal Cortex and Downstream Parahippocampal Regions in the Representation of Egocentric Boundaries

Highlights

- Egocentric boundary cells (EBCs) were described within the hippocampal region
- Using a GLM, “Pure” EBCs were identified mainly in the POR
- Conjunctive EBCs × HD cells were identified mainly in the PaS and MEC
- HD cells may drive the transformation from egocentric to allocentric coordinates

Authors

Xenia Gofman, Gilad Tocker, Shahaf Weiss, ..., Edvard I. Moser, Genela Morris, Dori Derdikman

Correspondence

derdik@technion.ac.il

In Brief

Gofman et al. describe pure egocentric boundary cells in the postrhinal cortex and dissociate it from other hippocampal regions using a GLM. This finding corroborates the idea that a coordinate transformation from egocentric to world-based coordinates, driven by head direction cells, underlies the formation of downstream border cells.



Dissociation between Postrhinal Cortex and Downstream Parahippocampal Regions in the Representation of Egocentric Boundaries

Xenia Gofman,^{1,6} Gilad Tocker,^{1,2,6,7} Shahaf Weiss,^{1,3,8} Charlotte N. Boccara,⁴ Li Lu,⁵ May-Britt Moser,⁵ Edvard I. Moser,⁵ Genela Morris,¹ and Dori Derdikman^{1,9,*}

¹Rappaport Faculty of Medicine and Research Institute, Technion – Israel Institute of Technology, Haifa 31096, Israel

²Gonda Multidisciplinary Brain Research Center, Bar Ilan University, Ramat Gan 52900, Israel

³Department of Zoology, Tel Aviv University, Tel Aviv 69978, Israel

⁴Institute of Basic Medical Sciences, University of Oslo, Oslo 0372, Norway

⁵Kavli Institute for Systems Neuroscience and Centre for Neural Computation, Norwegian University of Science and Technology, Trondheim 7030, Norway

⁶These authors contributed equally

⁷Present address: Department of Neurobiology, Northwestern University, Evanston, IL 60208, USA

⁸Present address: Max Planck Institute for Brain Research, Frankfurt am Main 60438, Germany

⁹Lead Contact

*Correspondence: derdik@technion.ac.il

<https://doi.org/10.1016/j.cub.2019.07.007>

SUMMARY

Navigation requires the integration of many sensory inputs to form a multi-modal cognitive map of the environment, which is believed to be implemented in the hippocampal region by spatially tuned cells [1–10]. These cells encode various aspects of the environment in a world-based (allocentric) reference frame. Although the cognitive map is represented in allocentric coordinates, the environment is sensed through diverse sensory organs, mostly situated in the animal's head, and therefore represented in sensory and parietal cortices in head-centered egocentric coordinates. Yet it is not clear how and where the brain transforms these head-centered egocentric representations to map-like allocentric representations computed in the hippocampal region. Theoretical modeling has predicted a role for both egocentric and head direction (HD) information in performing an egocentric-allocentric transformation [11–15]. Here, we recorded new data and also used data from a previous study [16]. Adapting a generalized linear model (GLM) classification [17], we show that the postrhinal cortex (POR) contains a population of pure egocentric boundary cells (EBCs), in contrast with the conjunctive EBCs × HD cells, which we found downstream mostly in the parasubiculum (PaS) and in the medial entorhinal cortex (MEC). Our finding corroborates the idea of a brain network performing an egocentric to allocentric transformation by HD cells. This is a fundamental building block in the formation of the brain's internal cognitive map.

RESULTS AND DISCUSSION

We recorded single units from visual area V2, the postrhinal cortex (POR), the parasubiculum (PaS), and the dorsal presubiculum (dPrS) in Long-Evans rats (N = 19) while they performed open-field foraging in square and circular arenas. We identified in these areas a cell type, which encodes the boundaries of the environment in an egocentric reference frame. We subsequently analyzed a large dataset of PaS, dPrS, and medial entorhinal cortex (MEC) units, previously published by Boccara et al. [16], recorded in a similar task. In total, we analyzed 2,183 single units: 453 in V2; 106 in POR; 606 in dPrS; 375 in PaS; and 119 in MEC, as well as 524 units that were recorded in border areas and thus were anatomically unclassified. All recorded units underwent a commonly used analysis procedure in allocentric coordinates, in which 2D firing rate maps and head direction (HD) polar plots were calculated (see [STAR Methods](#)). In addition, the units underwent an analysis in egocentric coordinates, in which their firing rate was calculated as a function of the rat's distance from the wall at different egocentric angles ([Figures 1A–1F](#); see [STAR Methods](#)). Some cells showed egocentric tuning, and the allocentric tuning was missing ([Figure 2A](#)). Other cells showed a conjunctive representation of allocentric tuning (such as HD and position) and egocentric tuning to walls as boundaries ([Figure 2B](#)). Statistical significance of the egocentric tuning of each cell was estimated by two distinct and unbiased methods: the first classification method was a generalized linear model (GLM) (or linear-nonlinear-Poisson [LNP] model) [17] with an adaptation of an addition of egocentric boundary dimensions (see [STAR Methods](#)). The GLM enabled us to examine the extent to which egocentric coding was independent of allocentric variables (such as position, HD, and speed). Cells that exhibited a significant egocentric component were classified as egocentric boundary cells (EBCs). As a second method, we used a shuffling procedure, in which spikes were randomly shifted in time (see [STAR Methods](#)).



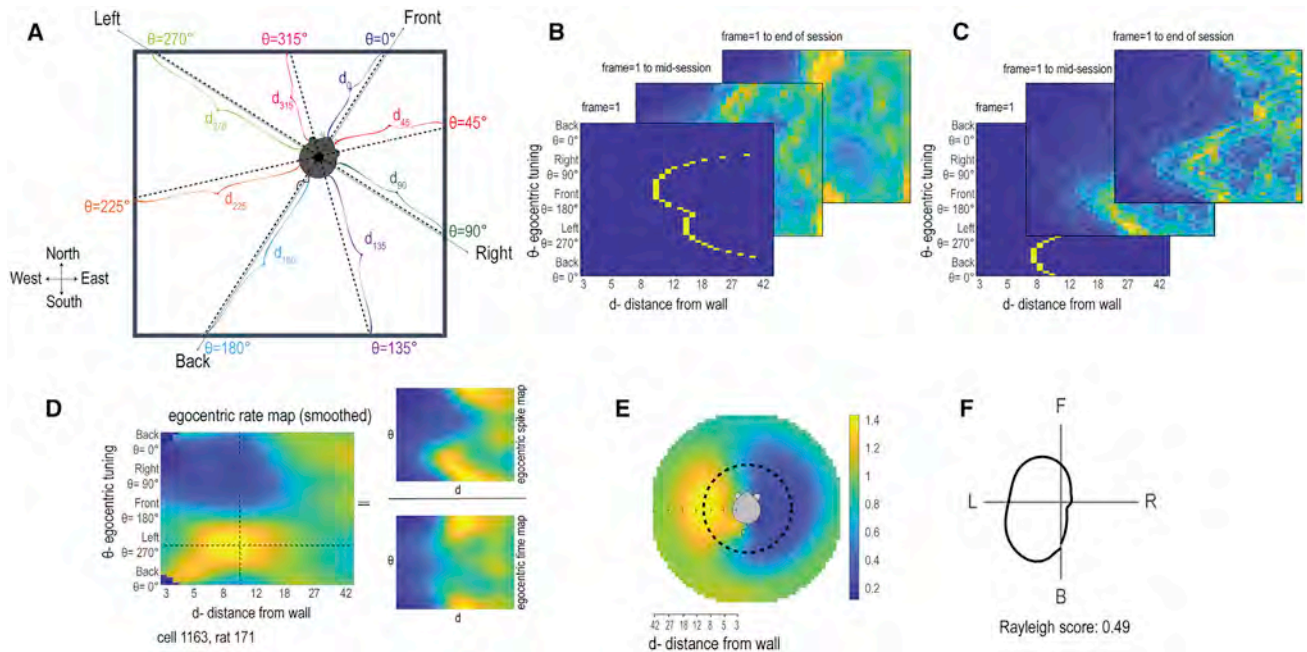


Figure 1. Egocentric Analysis for Egocentric Boundary Cells (EBCs)

(A) In an allocentric reference frame, the rat's position in the arena was encoded in world-centered coordinates. For example, here, the rat was in the northeast quadrant near the center of the box. In an egocentric reference frame, the rat's position in the arena was encoded in an egocentric coordinate system. In this example, the closest wall was on the front left of the rat. For every egocentric angle from the rat ("Θ"), we calculated the distance ("d") of the wall in that direction. (B) Egocentric time map: for each time frame, the rat's distance to each point on the border of the arena at given egocentric angles was summed up in polar coordinates (egocentric angle versus distance). (C) Egocentric spike map, produced in a similar way to (B), using the spike times.

(D) Egocentric firing map was calculated by dividing the spike map by the time map. The vertical and horizontal dashed lines represent the optimal wall distance and angle, chosen according to the bin with the maximal firing rate. (E) Egocentric firing map in Cartesian coordinates; the rat is located in the center of the firing map, and the activity of the firing map represents the activity of one cell in response to the appearance of the wall relative to the rat at a given egocentric direction and distance. The yellow area in the firing map indicates that this cell was mostly active when the borders of the arena were 10 cm to the left of the rat. The black ring represents the dashed line from (D). The radius was chosen according to the distance from the rat to the bin with the maximal firing rate. Note that in (B)–(E) distance is shown in logarithmic scale. (F) Polar plot of firing rates in different egocentric angles for the preferred distance (black ring) (E). The cell in this example was tuned to a boundary on the left of the rat.

Overall, the GLM was successful in fitting a model to 968/2,183 cells, of which 301 cells had an egocentric component (Figure 3A).

EBCs were found in both square and circular environments (Figure S1A). All egocentric angles were represented, with some overrepresentation of the front hemifield (front right and front left [$n = 156$] versus back, back right, and back left [$n = 62$]; $\chi^2 [1] = 40.53$; $p < 0.0001$) (Figure 3B). No difference was observed in the distributions of egocentric angles encoding contralateral (122/301) versus ipsilateral (105/301) hemifields between the hemispheres ($\chi^2 [1] = 1.27$; $p = 0.26$) (Figure S1B). Additionally, we did not see a difference in the direction of egocentric tuning between "pure" EBCs versus conjunctive EBCs \times HD cells ($\chi^2 [7] = 13.12$; $p = 0.11$), (Figures S1C and S1D for "pure" vs. conjunctive, respectively). Sixty-eight percent of the recorded EBCs ($n = 206$) responded to walls that were in close proximity to the rat (≤ 15 cm), and the rest ($n = 95$; 32%) responded to walls at larger distances (>15 cm) (Figure 3C). Ninety-one percent of EBCs ($n = 274$) showed stable egocentric border representations within the recording session (see STAR Methods). The existence of cells that represent walls at large distances from the animal

may indicate that EBCs also integrate information from modalities other than the somatosensory one. Additionally, 14% of cells recorded in dark sessions were classified as EBCs (Figure S1E; Table S2), compared with 30% classified as EBCs in sessions recorded in the light on the same dates (Table S3). We next examined the proportions of EBCs in the various brain regions. The POR differed from the other recorded regions (V2, dPrS, PaS, and MEC) in its high percentages of pure EBCs ($\chi^2 [4] = 128.8$; $p < 0.0001$). Indeed, the most prominent population of pure EBCs was found in the POR, where 22% of the cells were classified as pure EBCs ($n = 23$). In V2, only 5% of cells were classified as EBCs ($n = 20$), a percentage that is close to the chance level of the GLM classification. In dPrS, PaS, and MEC, less than 1% of cells were identified as pure EBCs (Figure 3D). The recorded structures also differed in their proportions of conjunctive EBCs \times HD cells ($\chi^2 [4] = 135.04$; $p < 0.0001$). Populations of EBCs \times HD cells were found in the POR ($n = 34$; 33%), PaS ($n = 21$; 6%), and in the MEC ($n = 14$; 12%), and to a lesser extent in the dPrS ($n = 21$; 4%). No conjunctive cells were identified in V2 (Figure 3D). Our results on conjunctive EBCs \times HD cells are consistent with conjunctive border \times HD cells documented in the

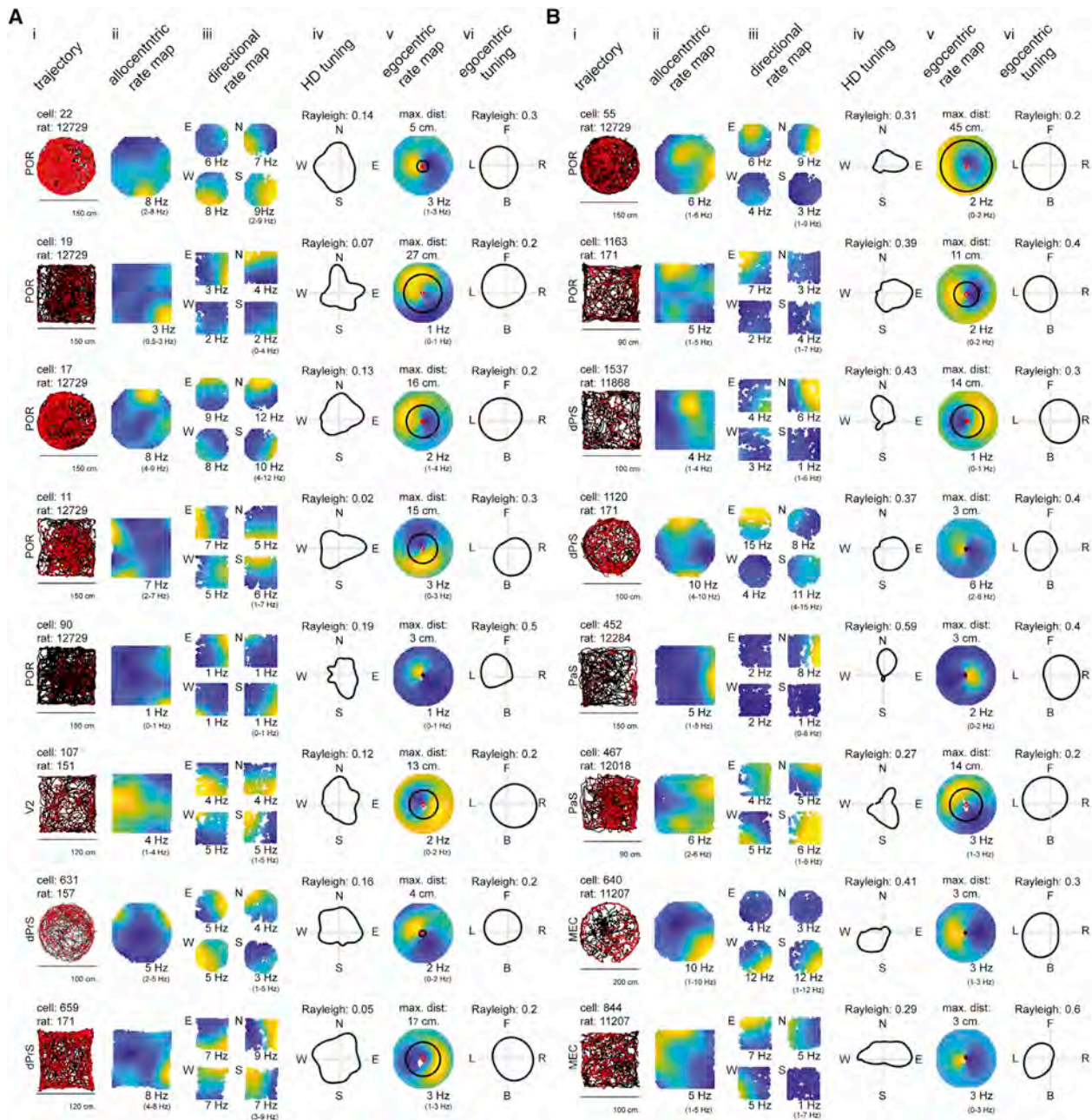


Figure 2. Examples of Cells Classified as “Pure” EBCs and Conjunctive EBCs × HD Cells

(A) Pure EBC examples in POR, V2, and dPrS. (i) The trajectory of the rat in the arena is represented by the black line; the red dots represent spike locations. The size of the arena is registered below. (ii) Allocentric firing map of the rat in the arena is shown. The yellow color is for the maximal firing rates; the blue is for the lowest. Maximal firing is noted below map. Range of color map is given in parenthesis. (iii) Allocentric rate maps for trajectories of the rat for north (N), south (S), east (E), and west (W) heading direction are shown. Color scale is as in (ii). (iv) HD polar rate map of the cell is shown. Rayleigh score is for HD. (v) Egocentric rate map is shown. The maximal distance is half the size of the arena in (ii), in logarithmic scale. The preferred distance is given in cm. Color scale is as in (ii). (vi) Egocentric tuning curve of the cell is shown. Rayleigh score is for egocentric tuning.

(B) Examples of conjunctive EBCs × HD cells recorded in POR, dPrS, PaS, and MEC. The organization of this panel is similar to that of (A).

See also [Figures S1](#) and [S3](#) and [Tables S2](#) and [S3](#).

dPrS in a previous study [18], which demonstrated very different firing rates when the rats were running in opposite directions along the walls. To test the directionality of the conjunctive cells, we examined the HD Rayleigh scores for cells that were classified as EBCs × HD cells in the different regions. In POR, the mean

Rayleigh score of these cells was 0.13, much lower than in the dPrS (0.55), the PaS (0.48), and the MEC (0.48; one-way ANOVA; $F[3] = 27.89$; $p < 0.0001$). Post hoc comparison revealed that the value in the POR was significantly different from other groups ($p < 0.0001$; Bonferroni corrected). From this we conclude

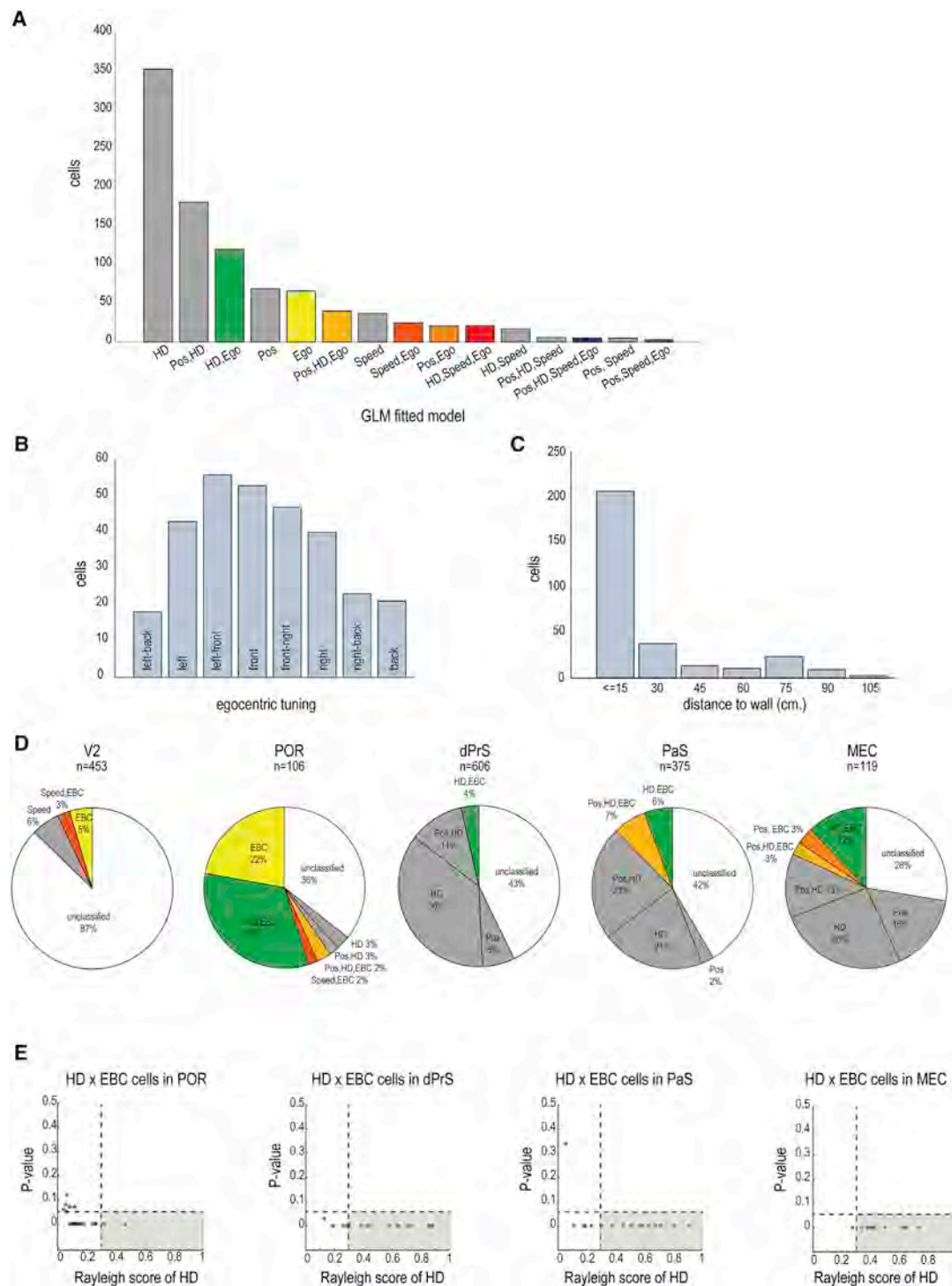


Figure 3. Population Statistics for Egocentric Cells Using the GLM Model

(A) Distribution of the selected models for the 969 cells identified by the GLM model approach.

(B) Directional tuning of EBCs according to their preferred egocentric directions.

(C) EBC tuning to the rats' distances from the wall.

(D) Cell class distribution in different anatomical regions (from left to right: V2, POR, dPrS, PaS, and MEC). Cell classes forming less than 1% of the population are not shown.

(E) HD Rayleigh score (x axis) and the p value of original HD cell (y axis) for cells classified as EBCs x HD cells by the GLM. Each dot is a cell; the gray area represents the commonly used classification for HD cells.

See also [Figures S2–S4](#).

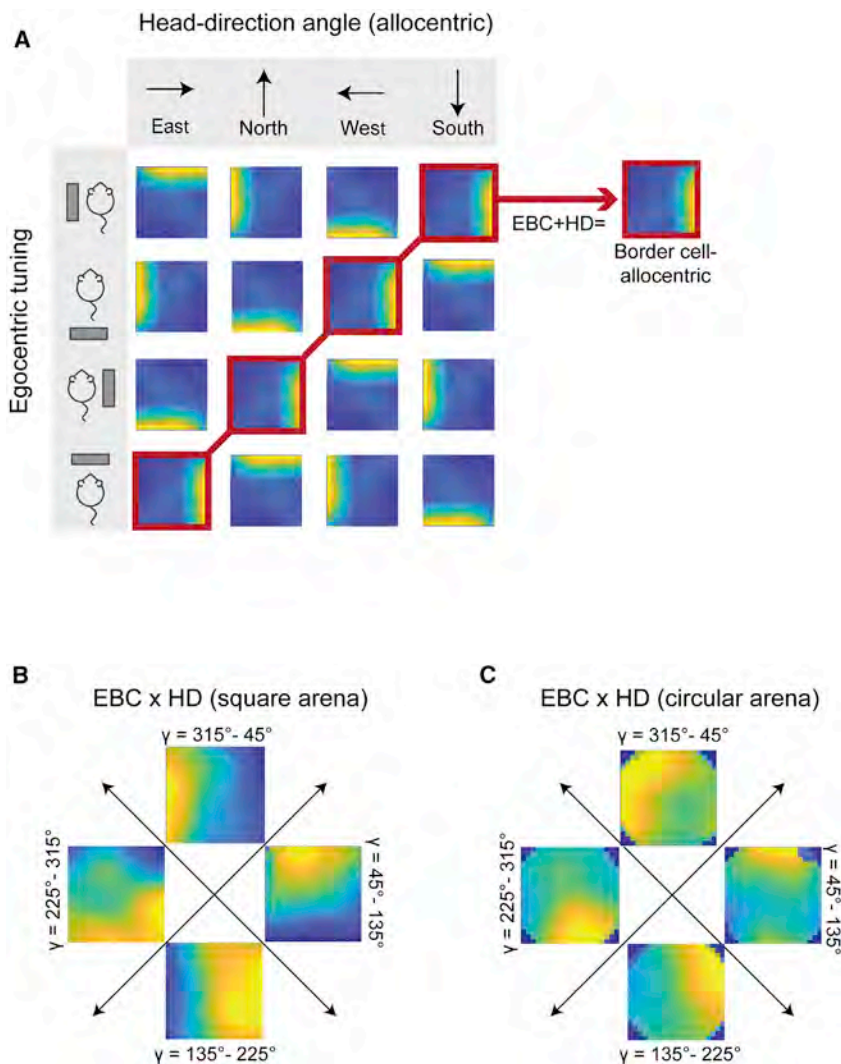


Figure 4. Generation of Border Cells: Model Sketch and Real Data

(A) Theoretical model sketch for the generation of border cells. 16 schematic EBCs \times HD cells are arranged in a matrix. Rows represent the egocentric tuning of the cells, and columns represent the allocentric tuning of their HD component. As an example, we depicted the formation of an allocentric eastern border cell with no HD component, generated from the conjunction of four cells with different EBC and HD properties (red frame).

(B) Recorded cells were used as building blocks for the model; for each conjunctive EBC \times HD cell recorded in the square arena, we calculated the angle γ resulting from the conjunction of its allocentric HD angle and egocentric EBC angle. We then divided the resulting angles into four quadrants and summed all allocentric rate maps corresponding to each range of angles.

(C) Same procedure as in (B) for the circular arena case.

See also Figure S4.

that there was a lower modulation of the HD signal in EBCs in the POR relative to the other regions (Figure 3E).

Altogether, this suggests a general picture in which, out of the regions we recorded, pure EBCs were found in the POR, and conjunctive EBCs \times HD cells were found mostly in the MEC, the PaS, and, with lower HD Rayleigh scores, also in the POR. The data reflect different levels of integration of egocentric and HD information in different parahippocampal regions. We analyzed the same population of cells using a shuffling analysis, and the relation between pure EBCs and conjunctive EBCs \times HD cells in the different areas resembled the results from the GLM classification (compare Figure S2 to Figure 3D). Our findings thus indicate a dissociation of the POR, containing many EBCs, with the PaS and the MEC (and a small portion in the dPrS), containing mostly conjunctive EBCs \times HD cells. The POR has extensive anatomical connections with visual and parietal cortices [19], which both encode information in an egocentric reference frame [20, 21]. Based on our results and preliminary anatomical evidence from the Witter group (T. Doan et al., 2018, FENS conference), we propose that a main route of information transformation from egocentric to

allocentric representation of borders in this system occurs in the known pathway between sensory and parietal cortices to the POR and from there to the PaS and the MEC. Recent evidence shows the existence of an egocentric representation in the LEC and the dorsomedial striatum, suggesting that egocentric information may also be routed to these regions [22, 23]. Theoretical studies have used border (or boundary vector) cells to explain the emergence of other spatially tuned cells [24, 25]. However, the formation of border cells is itself poorly understood. Previous models have suggested that HD cells can participate in the generation of an egocentric-allocentric

transformation in various regions [11, 14, 26, 27]. Following these models, we propose that allocentric border cells may be formed by the integration of conjunctive EBCs \times HD cells, with different combinations of egocentric boundary tuning and HD selectivity (Figure 4A). EBCs \times HD cells could, in turn, be formed by combining inputs from HD cells and pure EBCs. The EBCs that we recorded in the POR and the EBCs \times HD cells that we recorded in the PaS and MEC could represent the stages of such an integration process. To explore the feasibility of this process, we first simulated generation of EBCs \times HD cells by using the tuning curves of recorded HD cells as gates for firing of pure EBCs from our data. As one would expect, we obtained a population of EBCs \times HD cells (Figures S4C and S4D; STAR Methods). We further examined the feasibility of the suggested egocentric-to-allocentric transformation by calculating the combined sum of angles of the preferred egocentric angle and the HD angle of conjunctive EBCs \times HD cells. We then pooled the allocentric rate maps of cells with a similar range of calculated angles (representing north, east, south, and west). Indeed, the firing map that was established for each range of angles showed tuning to a specific border of the arena in an allocentric reference

frame (Figures 4B and 4C; STAR Methods). We suggest that egocentric sensory inputs entering the system feed into EBCs in the POR, which are in turn combined with the HD signal to form a conjunctive representation in EBCs \times HD cells. The organized summation of such information could lead to the downstream formation of allocentric border cells observed in the dPrS, PaS, and the MEC.

Our results demonstrate an egocentric spatial representation upstream of and within the hippocampal region, supporting the notion that the EBCs play a role in the transformation between egocentric and allocentric reference frames using the HD signal [11, 14, 26, 27]. This indicates an additional role for the HD cells in the navigation system: they are not only used as an internal compass but also play a pivotal role in the transformation of egocentric signals into the allocentric cognitive map. Future work is needed to establish this role of HD cells and the role of egocentric representations in the formation of other spatially tuned cells. The current and future work will set a foundation for understanding the formation of the cognitive map through coordinate transformations in the brain.

STAR★METHODS

Detailed methods are provided in the online version of this paper and include the following:

- KEY RESOURCES TABLE
- LEAD CONTACT AND MATERIALS AVAILABILITY
- EXPERIMENTAL MODEL AND SUBJECT DETAILS
 - Subjects and surgery
- METHOD DETAILS
 - Apparatus
 - Training procedures
 - Data collection
 - Histology
- QUANTIFICATION AND STATISTICAL ANALYSIS
 - Spatial analysis
 - Details on the GLM model
 - Simulations
- DATA AND CODE AVAILABILITY

SUPPLEMENTAL INFORMATION

Supplemental Information can be found online at <https://doi.org/10.1016/j.cub.2019.07.007>.

ACKNOWLEDGMENTS

The research was supported by the Israel Science Foundation personal grants 2344/16 and 2655/18, by a Rappaport Institute grant, by the Allen and Jewel Prince Center for Neurodegenerative Disorders of the Brain grant, and by a joint Technion-Weizmann Adelis Foundation grant. We thank Cindy Cohen for proofreading. We thank Ximena Velasquez for her assistance with histology. We thank Thanh Doan for advice on anatomy. We thank Chen Elbak and Irina Reiter for help with experiment administration. We thank members of the Derdikman lab for ongoing technical assistance and discussions.

AUTHOR CONTRIBUTIONS

Conceptualization, D.D., G.T., and X.G.; Methodology, X.G., G.T., and D.D.; Software, X.G., S.W., and G.T.; Investigation, X.G., G.T., and D.D.; Data Curation, X.G., C.N.B., G.T., S.W., and L.L.; Writing – Original Draft, X.G. and G.T.;

Writing – Review & Editing, D.D., G.M., C.N.B., M.-B.M., and E.I.M.; Visualization, X.G.; Supervision, D.D.; Funding Acquisition, D.D.

DECLARATION OF INTERESTS

The authors declare no competing interests.

Received: December 2, 2018

Revised: June 11, 2019

Accepted: July 1, 2019

Published: August 1, 2019

REFERENCES

1. O'Keefe, J., and Nadel, L. (1978). *The Hippocampus as a Cognitive Map* (Oxford University).
2. McNaughton, B.L., Battaglia, F.P., Jensen, O., Moser, E.I., and Moser, M.B. (2006). Path integration and the neural basis of the 'cognitive map'. *Nat. Rev. Neurosci.* 7, 663–678.
3. Derdikman, D., and Moser, E.I. (2010). A manifold of spatial maps in the brain. *Trends Cogn. Sci.* 14, 561–569.
4. O'Keefe, J., and Dostrovsky, J. (1971). The hippocampus as a spatial map. Preliminary evidence from unit activity in the freely-moving rat. *Brain Res.* 34, 171–175.
5. Taube, J.S., Muller, R.U., and Ranck, J.B., Jr. (1990). Head-direction cells recorded from the postsubiculum in freely moving rats. I. Description and quantitative analysis. *J. Neurosci.* 10, 420–435.
6. Derdikman, D., and Knierim, J.J. (2014). *Space, Time and Memory in the Hippocampal Formation* (Springer).
7. Hafting, T., Fyhn, M., Molden, S., Moser, M.B., and Moser, E.I. (2005). Microstructure of a spatial map in the entorhinal cortex. *Nature* 436, 801–806.
8. Solstad, T., Boccara, C.N., Kropff, E., Moser, M.B., and Moser, E.I. (2008). Representation of geometric borders in the entorhinal cortex. *Science* 322, 1865–1868.
9. Lever, C., Burton, S., Jeewajee, A., O'Keefe, J., and Burgess, N. (2009). Boundary vector cells in the subiculum of the hippocampal formation. *J. Neurosci.* 29, 9771–9777.
10. Savelli, F., Yoganarasimha, D., and Knierim, J.J. (2008). Influence of boundary removal on the spatial representations of the medial entorhinal cortex. *Hippocampus* 18, 1270–1282.
11. Byrne, P., and Becker, S. (2008). A principle for learning egocentric-allocentric transformation. *Neural Comput.* 20, 709–737.
12. Touretzky, D.S., and Redish, A.D. (1996). Theory of rodent navigation based on interacting representations of space. *Hippocampus* 6, 247–270.
13. Byrne, P., Becker, S., and Burgess, N. (2007). Remembering the past and imagining the future: a neural model of spatial memory and imagery. *Psychol. Rev.* 114, 340–375.
14. Milford, M.J., Wiles, J., and Wyeth, G.F. (2010). Solving navigational uncertainty using grid cells on robots. *PLoS Comput. Biol.* 6, e1000995.
15. Becker, S., and Burgess, N. (2001). Modelling spatial recall, mental imagery and neglect. In *Advances in Neural Information Processing Systems 13: Proceedings of the 2000 Conference*, T.K. Leen, T.G. Dietterich, and V. Tresp, eds. (MIT), pp. 96–102.
16. Boccara, C.N., Sargolini, F., Thoresen, V.H., Solstad, T., Witter, M.P., Moser, E.I., and Moser, M.B. (2010). Grid cells in pre- and parasubiculum. *Nat. Neurosci.* 13, 987–994.
17. Hardcastle, K., Maheswaranathan, N., Ganguli, S., and Giocomo, L.M. (2017). A multiplexed, heterogeneous, and adaptive code for navigation in medial entorhinal cortex. *Neuron* 94, 375–387.e7.
18. Peyrache, A., Schieferstein, N., and Buzsáki, G. (2017). Transformation of the head-direction signal into a spatial code. *Nat. Commun.* 8, 1752.

19. Burwell, R.D., and Amaral, D.G. (1998). Cortical afferents of the perirhinal, postrhinal, and entorhinal cortices of the rat. *J. Comp. Neurol.* **398**, 179–205.
20. Whitlock, J.R., Pfuhl, G., Dagslott, N., Moser, M.B., and Moser, E.I. (2012). Functional split between parietal and entorhinal cortices in the rat. *Neuron* **73**, 789–802.
21. Wilber, A.A., Clark, B.J., Forster, T.C., Tatsuno, M., and McNaughton, B.L. (2014). Interaction of egocentric and world-centered reference frames in the rat posterior parietal cortex. *J. Neurosci.* **34**, 5431–5446.
22. Wang, C., Chen, X., Lee, H., Deshmukh, S.S., Yoganarasimha, D., Savelli, F., and Knierim, J.J. (2018). Egocentric coding of external items in the lateral entorhinal cortex. *Science* **362**, 945–949.
23. Hinman, J.R., Chapman, G.W., and Hasselmo, M.E. (2019). Neuronal representation of environmental boundaries in egocentric coordinates. *Nature communications* **10**, 2772.
24. Hartley, T., Burgess, N., Lever, C., Cacucci, F., and O'Keefe, J. (2000). Modeling place fields in terms of the cortical inputs to the hippocampus. *Hippocampus* **10**, 369–379.
25. Barry, C., Lever, C., Hayman, R., Hartley, T., Burton, S., O'Keefe, J., Jeffery, K., and Burgess, N. (2006). The boundary vector cell model of place cell firing and spatial memory. *Rev. Neurosci.* **17**, 71–97.
26. McNaughton, B.L., Knierim, J.J., and Wilson, M.A. (1995). Vector encoding and the vestibular foundations of spatial cognition: neurophysiological and computational mechanisms. In *The Cognitive Neurosciences*, M.S. Gazzaniga, ed. (MIT), pp. 585–595.
27. Hinman, J.R., Dannenberg, H., Alexander, A.S., and Hasselmo, M.E. (2018). Neural mechanisms of navigation involving interactions of cortical and subcortical structures. *J. Neurophysiol.* **119**, 2007–2029.
28. Fisher, N.I. (1995). *Statistical Analysis of Circular Data* (Cambridge University).

STAR★METHODS

KEY RESOURCES TABLE

REAGENT or RESOURCE	SOURCE	IDENTIFIER
Chemicals, Peptides, and Recombinant Proteins		
PBS (10x)	Sigma-Aldrich	P5493-4L
Paraformaldehyde	Sigma-Aldrich	HT501128-4L
Buprenorphine	Vetmarket	0.3 mg/ml, 10 ml, http://www.vetmarket.co.il
Isoflurane	Vetmarket	http://www.vetmarket.co.il
Solvasol	Vetmarket	http://www.vetmarket.co.il
Experimental Models: Cell Lines		
Rats: Long-Evans HsdBlue:	Harlan - Envigo	3BLU:LE01
Software and Algorithms		
MATLAB v2017a/b, 2018a	MathWorks	https://www.mathworks.com/
Recording software: Cheetah v5.6	Neuralynx	http://neuralynx.com/
Spike sorting software	Neuralynx	SpikeSort3D
LabBook – documentation and actuator control software	Fellous lab website	http://amygdala.psychdept.arizona.edu/lab.html
Other		
Stereotaxic apparatus	David Kopf Instruments	Model #942
Lynx SX Recording platform	Neuralynx	http://neuralynx.com/
Gold pins	Neuralynx	large EIB Pins
Recording wires	California Fine Wire	Model:M283720 size: 17μm, Platinum 90% Iridium 10%
Head-stage tether	Neuralynx	HS-18
Head-stage connector	Omnetics	NPD-18-DD-GS
Electronic interface board (EIB)	Custom built by Rogat Enterprises	N/A
Microdrive	Custom built by Rogat Enterprises	N/A
Drive assembly mount for EIB	Custom built by Rogat Enterprises	N/A

LEAD CONTACT AND MATERIALS AVAILABILITY

This study did not generate new unique reagents.

Further information and requests for resources and reagents should be directed to and will be fulfilled by the Lead Contact.

EXPERIMENTAL MODEL AND SUBJECT DETAILS

Subjects and surgery

For the data acquired in the Derdikman lab, four adult male Long-Evans rats (healthy, drug-naive, 400–600 g, 4–8 months old, not involved in previous procedures) were implanted with a microdrive under isoflurane anesthesia (~2%) and buprenorphine analgesia. The microdrives (Rogat and Omnetics) contained four tetrodes (17-mm, 90% platinum 10% iridium); the electrode tips were platinum-plated to reduce electrode impedances to ~200 kΩ at 1 kHz.

The microdrive was mounted on a moveable assembly for recording neuronal activity and local field potentials in the visual area V2, postrhinal cortex ('POR'), dorsal presubiculum ('dPrS') and parasubiculum ('PaS') (0.5–0.8 mm anterior of transverse sinus; 4.2–4.6mm ML; 0.8–2.0 mm DV).

A ground screw was inserted into the frontal bone plate and attached by a wire to the microdrive during recording sessions. Rats were monitored for 1–2 weeks of recovery prior to recording and maintained above 85% of their free-feeding weight.

Rats were in a 12/12hr light/dark regime, dark period 10:00–22:00. Rats were held in 46.2 × 40.3 × 40.4 cm cages with sawdust bedding. All experimental procedures were approved by the Animal Care and Use Committee of the Technion – Israel Institute of Technology.

METHOD DETAILS

Apparatus

The experimental arena consisted of a black open-top plastic square box, 120 × 120 × 60 cm, and 90 × 90 × 60 cm. Some of the recording sessions were performed in a circular arena as well, with a diameter of 90 cm and height of 60 cm, and in the square arena, in full darkness, via an infrared camera (Neuralynx). A cue card was attached to one of the walls for orientation.

Training procedures

Rats were handled and then trained to forage in the arena; the foraging was motivated by randomly scattering chocolate sprinkles in the recording enclosures. The training was repeated until full coverage of the arena was observed.

Data collection

All data from the Derdikman lab were collected using the Digital Lynx SX data acquisition system (Neuralynx) at 32 KHz and Cheetah 5.6 software (Neuralynx). All signals were pre-processed with a bandpass filter of 600–6000 Hz. Single units were manually isolated into cell clusters using SpikeSort3D software (Neuralynx). The rats' position was tracked using two LEDs (red and green) mounted on a head-stage, connected to the implanted microdrive, or by using two infra-red LEDs, for tracking in the dark.

Rats were connected to the recording equipment and released in the center of the arena. The tetrodes were lowered in steps of 50 μ m until single neurons could be isolated at appropriate depths. When single units were detected, the rat performed an open field session in the square arena. Then, cells were analyzed with MATLAB and if relevant cells were detected, the rat was connected again to the recording equipment. If the cells from the first experiment were stable; the rat performed an additional open field task in a circular arena and in the square arena in full darkness. After each completed set of experiments, the tetrodes were moved further until new well-separated cells were encountered.

Histology

Rats were perfused with PBS (Sigma-Aldrich). Brains were removed and stored in 4% paraformaldehyde for 2–3 days at 4°C, then transferred to sucrose solutions of 30% over a period of 3–5 days. Following fixation, brains were sliced into 30 mm thick slices in a cryostat at –20°C. To identify tetrode traces, selected slices were treated with increasing gradients of ethanol solution to remove any fat in tissue, and then with decreasing gradients to rehydrate slice tissue. Finally, slices were stained with Cresyl violet to distinguish cell bodies.

QUANTIFICATION AND STATISTICAL ANALYSIS

All statistical analyses were conducted using MATLAB 2017b and MATLAB 2018a software.

In addition to the new data from the Derdikman lab, we analyzed previously published data by Boccara et al., (2010) [16] from dPrS, PaS and MEC. The data were recorded during open field tasks in square and circular arenas (for additional information on the methods, see ref. 16).

Spatial analysis

Allocentric rate map

The spatial rate map of each cell was computed by partitioning the arena into bins of 3 cm × 3 cm. Next, the spike-count per bin was computed and divided by the total time spent by the animal at the bin. The resulting rate map was then smoothed using a Gaussian kernel with standard deviation of $\sigma = 3$ bins.

Head direction

The rat's head direction was calculated for each video frame by computing the direction of the line perpendicular to the vector connecting the centers of the two light-emitting diodes on the rat's head (the color difference between the two diodes, green and red, enabled distinguishing forward from backward head-direction). The head-direction tuning of a neuron was computed by binning the data in 6° bins; the firing-rate in each bin was computed by dividing the number of spikes in that bin by the time the animal spent in the bin. The peak firing rate was defined as the highest rate in the head-direction tuning curve. The directionality of this tuning was quantified by computing the mean vector length of the circular distribution [28] (Rayleigh score). Only cells with a Rayleigh score ≥ 0.3 were classified as HD cells.

Border cells

Border cells were analyzed as described in Solstad et al., (2008) [8]. Briefly, border cells were characterized by identifying neighboring bins with firing rates that were higher than 0.3 times the maximum firing rate and covering a total area of a single wall. Border score range was between –1 (no border preference) and 1 (high border preference). We classified a cell as a border cell if its border score was ≥ 0.5 and the original border score was higher than 990/1000 of the shuffled ones (p value ≤ 0.01).

The shuffling procedure

The shuffling procedure was applied to determine the significance of each neuron's score. For each cell, the entire sequence of spikes was shifted in time by a random (uniformly-distributed) interval between 0.04 s and the duration of the session minus

0.04 s; If the range of shuffled spikes was within 30 s of the original times, a new time shift was drawn. The end of the session was wrapped to the beginning. This preserved the spike number and the temporal structure of the neuron's firing pattern but dissociated the time of spiking from the animal's original trajectory. This procedure was repeated 1000 times for each neuron; an original score higher than 990 of the shuffled ones classified the cell as a border cell (p value < 0.01).

Egocentric analysis

To compute the egocentric rate map for each cell, we first calculated the walls' egocentric location relative to the rat, throughout the session. We computed, at each moment in the session, the distance from the rat's position as estimated from the LEDs on its head to the environment walls in every direction. From these directions to the walls, we subtracted the animal's head direction at each moment (Figure 1A).

Subsequently, the full range of egocentric directions was partitioned into 6° slices and egocentric distances were partitioned in logarithmic scale, up to half the size of the arena. The firing rate of the cell in each bin was computed by dividing the number of spikes in that bin by the time the animal spent in the bin (Figures 1B and 1C). The resulting egocentric rate map was then smoothed using a Gaussian kernel with a standard deviation of $\sigma = 5$ bins. The bin with the highest firing rate was identified. The distance of the maximal bin was defined as the preferred distance to the wall, and the angle with the highest firing rate represented the preferred egocentric angle to the wall (Figures 1D–1F).

EBCs were classified as significant egocentric cells if their Rayleigh score was higher than 95% (95/100) of the shuffled distribution (“ p -value ≤ 0.05 ”). If the range of shuffling was within 30 s of the original times, a new time shift was drawn.

Stability within a session

To quantify the stability of EBCs within a session, each session was divided into two equal-length time segments. An egocentric rate map (polar coordinates) was calculated for the first and the second segment. Stability scores were calculated by computing the correlation of the calculated egocentric rate maps between the segments. The second segment was shuffled 100 times as described above. Cells with stability scores higher than 95% of the shuffled ones were defined as stable.

Details on the GLM model

To determine the parameters encoded by the neurons' activity, we fit a general linear model (GLM) to each neuronal activity sequence, modified from the LN model and code described in [17]. Briefly, the model aims to accurately describe the neuronal smoothed spike train r as an exponential function of the state of the animal, determined by the animals' position (P), head direction (H), speed (S) and egocentric location of the walls (Ego):

$$r = e^{\sum_i x_i^T w_i / dt}$$

Where r is a vector of instantaneous firing rates in T time bins of $dt = 40$ ms. The state vector x is composed of one to four variables $x_i \in \{0, 1\}$, weighted by the corresponding factors w_i . To prevent overfitting, we performed a cross validation procedure, where w_i was estimated on a subset of the data and testing for maximum log likelihood was performed on separate test dataset. This procedure was repeated 10 times. We tested separately for each of the following 15 models: four single factor ones (P, H, S, Ego), six double factors ($P \times H, P \times S, P \times Ego, H \times S, H \times Ego, S \times Ego$), four triple models ($P \times H \times S, P \times H \times Ego, P \times S \times Ego, H \times S \times Ego$), and a full model ($P \times H \times S \times Ego$). While the P, H , and S models were described in [17], our added egocentric component (Ego) is described in the following section.

Finally, we performed a one-sided signed rank test to the log likelihood values of each model, choosing the model with the smallest number of parameters, which accounted for the data significantly better than others ($p < 0.05$) [17]. For chosen model parameters, see Table S1.

Egocentric variable models and state vectors

To quantify the dependence of the cell's spiking activity on the egocentric location of the environment walls, we introduced the wall egocentric-location variable to the LN model (Ego). At each moment in time, each point in the environment walls had a specific distance and egocentric direction. This posed the problem of multiple animal-states at each time point, when considering the variable of the egocentric walls. To overcome this problem, we optimized the parameters of each egocentric direction as a distinct variable of the model. To compute the egocentric location of the walls, we first computed, at each moment in time, the distance and direction of each point on the walls from the animal's center of mass. From this direction, we subtracted the animal's head direction at each moment.

Then, the full range of egocentric directions was divided into 8 bins (45°). In addition, the full range of distances between the walls and the animal was distributed across a logarithmic scale and divided into 8 bins. Each bin of egocentric directions was considered a different variable of the model that varies in time by the wall's distance to the animal in that egocentric direction. That is, at each moment in time, the animal-state vector, for each egocentric direction, was denoted by a vector with a value of 0 on all elements, except for one element, which was set to 1, corresponding to the bin of the current wall's distance to the animal in this specific egocentric direction.

Only models containing all the egocentric directions, or none of them, were optimized and selected. i.e., a model with only some of the egocentric directions, and not others, was not selected. For examples of cells that were classified as pure egocentric or as conjunctive EBC \times HD, see Figure S3.

Simulations

Simulation of shifted spike train for POR data

To check the reliability of the GLM method in classifying cells with an egocentric component, we generated a population of cells (POR cells) with random spike trains and ran the GLM on the simulated data. To produce the simulated population, each cell's spikes were cyclically shifted in time, and the new shifted population was used. [Figures S4A and S4B](#) shows the results of the GLM classification on the simulated population.

Simulation of BC from EBC x HD cells

To examine the feasibility of our suggestion that BCs may be indeed generated as a combination of inputs from EBC x HD cells, as was suggested in [Figure 4A](#), we used 120 cells that were classified as EBC x HD cells by the GLM. For each cell, we calculated a summed angle (γ) that represents the combined value of HD angle (1° - 360°) and EBC angle (1° - 360°). $\gamma = \text{mod}((HD^\circ + EBC^\circ), 360)$. Then we summed up all allocentric rate maps (divided by their maximum firing rate) of EBC x HD cells within four given ranges for the summed angles: (1) from 315° to 360° and from 1° to 45° ; (2) from 45° to 135° ; (3) from 135° to 225° ; (4) from 225° to 315° ([Figures 4B and 4C](#)).

Simulation of EBC x HD cells from 'pure' EBC and HD cells

To simulate EBC x HD cells, we used our population of classified 'pure' EBCs. For each EBC, we randomly selected 8 HD cells from our dataset for the simulation of a new population of EBC x HD cells, as follows:

We used each HD cell in order to generate a probability of selecting spikes from a pure EBC and repeated this procedure 100 times. The simulated spike train was generated by selecting those bins which contained spikes occurring in more than 30% of the repetitions. We calculated the allocentric and egocentric properties of the simulated cells and used the GLM analysis to classify the population to cell types ([Figures S4C and S4D](#)).

DATA AND CODE AVAILABILITY

Data and custom MATLAB codes used to generate all analyses are available from the lead contact upon request.